

Three-integral multi-component dynamical models and simulations of the nuclear star cluster in NGC 4244

F. De Lorenzi^{1*}, Markus Hartmann², Victor P. Debattista^{3,4†}, A.C. Seth⁵, O. Gerhard⁶

¹ *Zürcher Hochschule für Angewandte Wissenschaften, Technikumstrasse 9, CH-8401 Winterthur, Switzerland*

² *Astronomisches Rechen-Institut, Zentrum für Astronomie der Universität Heidelberg (ZAH), Mönchhofstr. 12-14, 69120 Heidelberg, Germany*

³ *Jeremiah Horrocks Institute, University of Central Lancashire, Preston, PR1 2HE, UK*

⁴ *Visiting Lecturer, Department of Physics, University of Malta, Tal-Qroqq Street, Msida, MSD 2080, Malta*

⁵ *University of Utah, Salt Lake City, UT USA*

⁶ *Max-Planck-Institut für Ex. Physik, Giessenbachstraße, D-85741 Garching, Germany*

Draft, last update 3 December 2024

ABSTRACT

Adaptive optics observations of the flattened nuclear star cluster in the nearby edge-on spiral galaxy NGC 4244 using the Gemini Near-Infrared Integral Field Spectrograph (NIFS) have revealed clear rotation. Using these kinematics plus 2MASS photometry we construct a series of axisymmetric two-component particle dynamical models with our improved version of NMAGIC, a flexible χ^2 -made-to-measure code. The models consist of a nuclear cluster disc embedded within a spheroidal particle population. We find a mass for the nuclear star cluster of $M = 1.6^{+0.5}_{-0.2} \times 10^7 M_\odot$ within ~ 42.4 pc ($2''$). We also explore the presence of an intermediate mass black hole and show that models with a black hole as massive as $M_\bullet = 5.0 \times 10^5 M_\odot$ are consistent with the available data. Regardless of whether a black hole is present or not, the nuclear cluster is vertically anisotropic ($\beta_z < 0$), as was found with earlier two-integral models. We then use the models as initial conditions for N -body simulations. These simulations show that the nuclear star cluster is stable against non-axisymmetric perturbations. We also explore the effect of the nuclear cluster accreting star clusters at various inclinations. Accretion of a star cluster with mass 13% that of the nuclear cluster is already enough to destroy the vertical anisotropy, regardless of orbital inclination.

Key words: galaxies: nuclei – galaxies: star clusters: general – galaxies: spiral – galaxies: kinematics and dynamics – galaxies: formation – galaxies: individual: NGC 4244 – methods: numerical

1 INTRODUCTION

Studies of the centres of galaxies across the Hubble sequence have shown that they frequently host central massive objects such as massive nuclear star clusters (NCs) and supermassive black holes (SMBHs). NCs are present in roughly 75% of low and intermediate luminosity disc and elliptical galaxies (Böker et al. 2002; Côté et al. 2006). These NCs are intrinsically very luminous, with typical $M_I \sim -12$, and sizes similar to globular clusters ($r_{eff} \sim 5$ pc; Böker et al. 2004).

Two hypotheses have been offered to explain NC formation. One scenario envisages NCs forming in situ out of gas cooling onto the centre (Milosavljević 2004; Bekki et al. 2006; Bekki 2007). Alternatively, NCs may form from star

clusters merging at the centres of galaxies (Tremaine et al. 1975; Lotz et al. 2001; Capuzzo-Dolcetta & Miocchi 2008). Which hypothesis is correct determines whether NC growth is limited by the supply of star clusters from the host galaxy or regulated by feedback from in situ star formation (McLaughlin et al. 2006).

NCs exhibit several scaling relations. The luminosity of NCs correlates with that of their host galaxy (Böker et al. 2002; Côté et al. 2006; Erwin & Gadotti 2010). A number of studies also found that their mass, M_{NC} , correlates with the velocity dispersion of the host bulge, the $M_{NC} - \sigma$ relation (Ferrarese et al. 2006; Wehner & Harris 2006; Rossa et al. 2006). Early work found that this $M_{NC} - \sigma$ relation is parallel to the $M_\bullet - \sigma$ relation of SMBHs (Gebhardt et al. 2000; Ferrarese & Merritt 2000), with NCs being about $10\times$ more massive, at the same σ , as SMBHs. However recent work has questioned how comparable NCs and SMBHs are.

* E-mail: flavio.delorenzi@gmx.ch

† RCUK Academic Fellow

Erwin & Gadotti (2012a) find that NCs and SMBHs follow different relations, with SMBH masses correlated with properties of the bulge, while NCs seem to correlate better with properties of the entire host galaxy. Instead, both Leigh et al. (2012) and Scott & Graham (2012) show that there is an $M_{\text{NC}} - \sigma$ relation but with a significantly different slope than for SMBHs. Part of these differences may be due to the fact that the $M_{\bullet} - \sigma$ and $M_{\text{NC}} - \sigma$ relations depend on Hubble type (Greene et al. 2010; Erwin & Gadotti 2012b), and especially that SMBHs and NCs in late-type galaxies not following the same scaling relations as in early-types. It is therefore important to shed light on how mass accretes into the centres of the late-type galaxies.

It is generally thought that AGN feedback is responsible for the $M_{\bullet} - \sigma$ relation (e.g. Silk & Rees 1998; King 2003; Murray et al. 2005; Di Matteo et al. 2005; Sazonov et al. 2005; Springel et al. 2005; Johansson et al. 2009), but scenarios where this relation arises because the galaxy regulates SMBH growth (e.g. Burkert & Silk 2001; Kazantzidis et al. 2005; Miralda-Escudé & Kollmeier 2005) or purely indirectly (Haehnelt & Kauffmann 2000; Adams et al. 2001, 2003; Jahnke & Macciò 2011) have also been proposed. Therefore NC scaling relations hold the promise of illuminating the origin of SMBH scaling relations. The similarity of the $M_{\text{NC}} - \sigma$ and $M_{\bullet} - \sigma$ relations suggests that related processes may be at work in controlling their growth (e.g. McLaughlin et al. 2006).

Some galaxies host both a NC and a SMBH (Seth et al. 2008a,b; Graham & Spitler 2009) and their properties provide further constraints on the relation between the two. For instance Neumayer & Walcher (2012) found that NCs and SMBHs do not coexist at $M_{\bullet}/M_{\text{NC}} \gtrsim 100$, which they propose suggests that NCs are precursors of SMBHs. Constructing an $(M_{\bullet} + M_{\text{NC}}) - \sigma$ relation which includes the mass of both the NC and of the SMBH (Graham et al. 2011), Graham (2012) found a flatter relation than the $M_{\bullet} - \sigma$ relation.

Unlike SMBHs, the assembly history of NCs can be constrained from their morphology, stellar populations and kinematics. In late-type spirals, NCs have been found to consist of multiple stellar populations, typically a young population (< 100 Myr), and a dominant population older than 1 Gyr (Davidge & Courteau 2002; Schinnerer et al. 2003; Rossa et al. 2006; Walcher et al. 2006). The *Hubble Space Telescope* has revealed that the NCs of edge-on galaxies host multiple stellar populations associated with different morphological components (Seth et al. 2006). These NCs consist of young blue nuclear cluster discs (NCD) and older nuclear cluster spheroids (NCS). Optical spectra of the NC in the edge-on Scd galaxy NGC 4244 ($i \approx 90^\circ$), the nearest galaxy in the sample of Seth et al. (2006) ($D=4.37$ Mpc; Seth et al. 2005a), indicates the presence of multiple stellar populations, while near infrared spectroscopy showed that the NC is rapidly rotating (Seth et al. 2008b). Using N -body simulations Hartmann et al. (2011, hereafter H11) showed that the NC in NGC 4244 cannot have assembled more than half its mass via the accretion of star clusters. H11 also modelled the NC in NGC 4244 using two-integral JAM models (Cappellari 2008), obtaining a mass of $(1.1 \pm 0.2) \times 10^7 M_{\odot}$.

To help shed light on the formation of NCs in late-type galaxies, in this paper we study the NC in the nearby Sc galaxy NGC 4244. The outline of this paper is as follows.

Section 2 describes the observational data and how they are used in the dynamical modelling. Our modelling method, the χ^2 -M2M code NMAGIC based on de Lorenzi et al. (2007, 2008, 2009), is described in Section 3 including additional code development. We construct various axisymmetric particle models of the nuclear region of NGC 4244 in Section 4 using this improved code. The models consist of a NCD and NCS having separate mass-to-light (M/L) ratios. Using the best model as initial conditions for N -body simulations, we explore the evolution of the NC in Section 5. Section 6 discusses our results in the context of NC formation.

2 OBSERVATIONAL DATA

We begin by describing the photometry and how these data are deprojected to obtain a three dimensional luminosity density. After this, the integral-field kinematic data are presented. We adopt a distance to NGC 4244 of 4.37 Mpc (Seth et al. 2005b). At this assumed distance, $1''$ corresponds to 21 pc.

2.1 Photometry

Here we give a brief summary of the photometric data and its model representation, both described in detail in Seth et al. (2005a, 2008b).

The photometry consists of K -band data either from 2MASS or from the NIFS observations of Seth et al. (2008b). The main disc (MD) of NGC 4244 hosts at its centre a NC which is composed of a NCD and an oblate NCS. The K -band mass-to-light ratio M/L_K is estimated to be 0.5–0.75 for the galaxy as a whole (from integrated colours taken from LEDA [$B - V = 0.4 - 0.6$] combined with M/L from Bell et al. (2003)). The M/L_K of the NCD is in the range 0.1–0.25 based on Bruzual & Charlot (2003) models applied to the optical spectroscopy of Seth et al. (2006), which agrees well with the fitted luminosities for the disc in *HST*/ACS and NIFS bands. The NCS stellar populations are poorly constrained and a M/L_K between 0.5 and 1.2 is likely.

The surface brightness of NGC 4244 is decomposed into an axisymmetric three component model. The luminosity distributions of the MD and the NCD are modelled as projected edge-on exponential discs (e.g. van der Kruit & Searle 1981):

$$\Sigma(x, z) = \Sigma_0 \left(\frac{x}{h_r} \right) K_1(x/h_r) \text{sech}(z/z_0)^2, \quad (1)$$

where Σ_0 and h_r are constants, and K_1 is the modified Bessel function. The corresponding model parameters for the MD and NCD models are taken from Seth et al. (2005a) and Seth et al. (2008b), respectively.

On the other hand the NCS is represented using a Sérsic (1968) profile:

$$I(x, z) = I_e \exp(-b_n((R/R_e)^{1/n} - 1)), \quad (2)$$

where I_e is the surface brightness at the effective radius R_e , $b_n \simeq 1.992n - 0.3271$ and $R = \sqrt{x^2 + (z/q)^2}$ is the elliptical radius, with flattening q . Best fit parameters have been obtained from Seth et al. (2008b).

All models were convolved with a Gaussian point spread

COMP.	Σ_0 [L_\odot/pc^2]	ρ_0 [L_\odot/pc^3]	h_r [pc]	z_0 [pc]	q	I_e [L_\odot/pc^2]	R_e [pc]	n
MD	598	0.167	1783	469				
NCD	1.41×10^5	2.08×10^4	3.39	1.19				
NCS					0.81	8.73×10^3	10.86	1.68

Table 1. Best-fit parameters of the photometric three component model taken from Seth et al. (2005a, 2008b). The model consists of an exponential main disc (MD), an exponential nuclear cluster disc (NCD) and a Sérsic nuclear cluster spheroid (NCS).

function (PSF) of $0''.23$ FWHM during the fitting process, *cf.* Seth et al. (2008b). The best fit parameters are summarised in Table 1. The left panel of Figure 1, which presents the NCS model, shows its surface brightness, μ_K , and ellipticity, $\epsilon = 1 - q$, profiles.

2.1.1 Deprojection

To compute the three dimensional luminosity distribution, each component of the surface brightness model is deprojected individually. The edge-on deprojection of an axisymmetric system is unique (Rybicki 1987). The surface-brightness profile of Equation 1 corresponds to an exponential disc, so the deprojection is readily given by (*e.g.* van der Kruit & Searle 1981):

$$\rho(R, z) = \rho_0 \exp(-R/h_r) \text{sech}(z/z_0)^2, \quad (3)$$

where $\rho_0 = \Sigma_0/(2h_r)$, and Σ_0 , h_r and z_0 are as in Equation 1. Their values are given in Table 1.

Unlike the surface brightness profile of an exponential disc, the Sérsic profile of the NCS cannot be deprojected in closed form. We therefore use the program of Magorrian (1999) to numerically deproject the surface brightness distribution of the NCS. The program finds a smooth axisymmetric density distribution consistent with the surface brightness distribution for the specified inclination angle (here edge-on, *i.e.* 90°), by imposing that the solution maximises a penalised likelihood. Because the deprojection is computed numerically and tabulated on a grid, the reprojected surface brightness profile may not match the Sérsic one perfectly. A comparison of the NCS Sérsic photometric model and its edge-on deprojection reprojected onto the sky plane, seen in the left panels of Figure 1, shows that the numerical deprojection is in fact very reliable. The right panel presents iso-density contours in the meridional plane of the NCS obtained with Magorrian (1999)’s code.

2.2 Kinematic Data

The integral-field NIFS kinematic data we use in the modelling were presented in Seth et al. (2008b) and consist of velocity, velocity dispersion and the higher order Gauss-Hermite moments h_3 and h_4 (van der Marel & Franx 1993; Gerhard 1993). The NIFS field-of-view extends to $\pm 1.5''$ along each direction, but the usable data is within $\pm 1.0''$. In this field-of-view, the positions of the “spaxels” within which spectra were taken define a grid of $63 \times 71 = 4473$ cells, which serves as the basis grid for Voronoi bins for which the velocity, velocity dispersions, h_3 and h_4 are given.

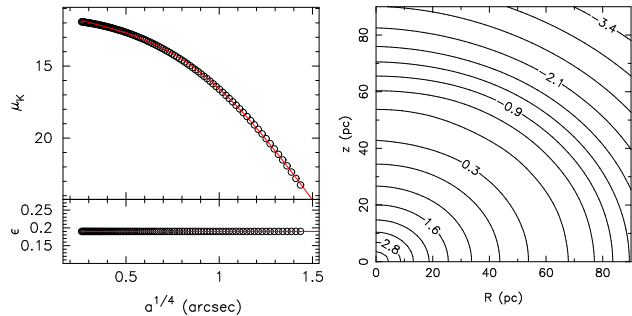


Figure 1. Left: Comparison of the NCS Sérsic photometry with the reprojected three dimensional luminosity model. The data points correspond to the NCS Sérsic profile, which was derived via a morphological fit. The solid line shows the model projected onto the sky plane. The upper panel shows the surface brightness, μ_K , and the lower one shows the ellipticity, $\epsilon = 1 - q$. Right: Iso-density contours of the NCS in the meridional plane. The luminosity density was obtained by an edge-on deprojection of the NCS Sérsic surface brightness. The contour labels are given in units of $\log_{10} L_\odot \text{pc}^{-3}$.

3 METHODS

We construct a range of dynamical models for the NC of NGC 4244. These models consist of a disc and a spheroidal particle population representing the NCD and NCS respectively. We use an adapted version of the flexible χ^2 -made-to-measure (M2M) particle code NMAGIC described in de Lorenzi et al. (2007, 2008). This section describes a few ingredients required to construct dynamical M2M models and presents further development of NMAGIC compared with our previous work in de Lorenzi et al. (2007, 2008).

3.1 Model observables

The central luminosity volume density of the NCS is about a million times larger than that of the main disc (Seth et al. 2008b). Thus the NCS dominates the luminosity distribution in the central region out to the edge of the observational data, allowing us to neglect the luminosity distribution of the main disc when computing the photometric observables. At a distance $R = 30$ pc from the centre, the luminosity density in the equatorial plane of the NCS is still about 100 times that of the MD.

We compute separate spherical harmonic coefficients A_{lm} for the density of the NCD and the NCS. The corresponding errors are inferred following a Monte-Carlo procedure described in de Lorenzi et al. (2008), in which the A_{lm} ’s are computed many times from random rotations

about arbitrary axes of a suitable particle realisation. Here, we used the isotropic particle model generated from the major-axis density profiles of the NCS and NCD components, described in Section 3.2 below. The A_{lm}^{NCD} and A_{lm}^{NCS} constrain the photometry of the disc and spheroidal particle populations, respectively. We use even A_{lm} ’s up to $l_{\text{max}} = 8$ in 40 radial bins, unevenly spaced, for a total of $N_{\text{Alm}} = 2000$ photometric constraints. The grid starts at $r_{\text{min}} = 0''.0001$ (0.002 pc) and extends to $r_{\text{max}} = 2''$ (42.4 pc).

The NIFS kinematic data (velocity v , dispersion σ , $h3$ and $h4$) are bi-symmetrised by adopting a point-symmetric reflection with respect to the centre of the galaxy, as described in de Lorenzi et al. (2009), followed by a reflection about the major axis. The resulting data within $\pm 0.7''$ are shown in the upper panel of Figure 6. As kinematic observables we use luminosity-weighted Gauss-Hermite coefficients h_1 up to h_4 (Gerhard 1993; van der Marel & Franx 1993; de Lorenzi et al. 2008) and the luminosity itself (corresponding to h_0) within the field-of-view, for a total of $N_{\text{kin}} = 365$ kinematic observables (73 Voronoi bins times 5 sets of Gauss-Hermite coefficients). These are used to constrain the particle system as a whole, without distinguishing between NCD and NCS populations. The particle model is seeing convolved with a Gaussian PSF having a FWHM of $0''.23$ (5 pc) by means of the Monte-Carlo method presented in de Lorenzi et al. (2008): When the model kinematics are computed, each particle is temporarily replaced by N_{pp} pseudo particles with randomly selected positions having probabilities given by the PSF. In the present work, we adopted $N_{\text{pp}} = 5$.

3.2 Initial conditions

We set up *spherical* initial conditions using the major-axis density profile of the NCS. Setting $M/L_K = 1$, the mass density is normalised to unit mass and the self-consistent gravitational potential is computed. Following Gerhard (1991), the isotropic distribution function is computed and used to generate a set of equal mass particles as in Debattista & Sellwood (2000). Finally, 30% of the particles are randomly assigned to the "disc" population. We produced two realisations of these initial conditions, a low resolution one with 0.75M particles which allowed us to explore parameter space quickly and a higher resolution version with 6M particles.

3.3 Gravitational potential

The M2M method works by adjusting the weights of individual particles while they are evolved along their orbits. For this orbit integration the gravitational potential of the system is needed. This section details the methods used to construct the dynamical models presented in Section 4 below. In brief, low resolution models (M1) are built using an FFT method for the potential. Then high resolution models without (M2) and with intermediate mass black holes (IMBHs) (M3–M8) are built with the potential computed on a spherical mesh of spherical harmonics (Sellwood 2003).

We assume that the mass distributions of the MD, NCD and NCS follow their luminosity distributions J_i ($i \in \{\text{MD},$

NCD, NCS}). For a constant mass-to-light ratio M/L_i , the corresponding mass density is $\rho_i = (M/L_i)J_i$, with J_i the deprojection given in Section 2.1.1.

The potential in models M1 was obtained on a Cartesian grid. Each Cartesian grid consists of $N = 128^3$ grid cells. The NC grid extends to ± 50 pc along each direction, whereas the MD grid extends to ± 3000 pc. This allows us to resolve the scale-heights of the MD and the NCD and the half-mass radius of the NCS. The potential on each grid is calculated using the Fourier convolution theorem. We assign to each mesh point a mass from the corresponding density distribution. The potential is then obtained by a convolution with the Greens function. We employ the FFT method of Press et al. (1992) to perform the convolution.

We pre-compute the individual gravitational potentials Φ_i^{M1} generated by J_i , for unit mass-to-light. This procedure allows us to quickly obtain the total gravitational potential for any choice of M/L_i through a weighted sum $\Phi = \sum_i M/L_i \Phi_i^{M1}$, which is kept constant for each model run.

For a modelling run, we initially tabulate $\Phi_i = M/L_i \Phi_i^{M1}$ on individual Cartesian grids. Forces at grid points are computed by finite differences. Individual particle accelerations are then approximated by a cloud-in-cell scheme (Hockney & Eastwood 1988) to interpolate the grid point forces to the particle position.

For models in the series M2–M8 we use a spherical harmonic potential solver as described in Sellwood (2003). We use the disc and spheroid particle populations (particle weights are converted to mass via the associated M/L_K) to calculate the gravitational potential of the entire particle system. Thus, the contribution of the MD is neglected. As discussed at the end of Section 2.1.1 the error associated with this approximation is expected to be very small. For models using the spherical harmonic potential solver, the potential is updated after every M2M correction step (and temporally smoothed). We use potential expansion coefficients up to $l_{\text{max}} = 8$ with 300 (unevenly spaced) radial bins to $r_{\text{max}} = 200$ pc. The width of the innermost bin is 0.2 pc and of the outermost bin is 4.2 pc, which is still smaller than the FWHM of the PSF.

3.4 Resampling a particle model

We use the final particle dynamical model as initial conditions for N -body simulations. In order to do this, it is best that the particles have a narrow range of masses; this ensures both higher effective mass resolution and a lower artificial two-body relaxation rate. The models are therefore built using the re-sampling technique described by Dehnen (2009). This section closely follows Dehnen (2009) work. We generate the models using a flat weight prior $\hat{w} = N^{-1}$. The particle models are re-sampled every 100 M2M correction steps if the ratio of largest to smallest particle weight is $\max\{w_i\}/\min\{w_i\} > 10$. Because we do not normalise total weight (it is only constrained by the observables, in particular by A_{00}), the weight of a re-sampled particle is set to $w_k = N^{-1} \sum_k w_{i,\text{old}}$. The phase-space coordinates $(\mathbf{x}_k, \mathbf{v}_k)$ of the k^{th} re-sampled orbit are set to the i^{th} original trajectory if

$$C_i < \bar{\gamma}(k - 1/2) \leq C_{i+1}, \quad i, k \in [1, N] \quad (4)$$

with mean relative normalised weight $\bar{\gamma} = N^{-1} \sum_i \gamma_i$, cumulative relative normalised weight $C_i = \sum_{k \leq i} \gamma_k$ and $\gamma_i = w_i/\bar{w}$ the relative weight. Orbits with $\gamma_i < \bar{\gamma}$ are re-sampled at most once, whereas orbits with $\gamma_i > \bar{\gamma}$ produce at least one copy. If a trajectory gets re-sampled, the first copy gets the phase-space position of the original particle. For additional copies we randomise positions $(x \pm d, y \pm d, z \pm d)$ with $d = (x^2 + y^2)^{1/2}/100$ exploring the eight distinct combinations of plus and minus signs. The position of any additional copy is set to $(x + r_x d, y + r_y d, z + r_z d)$ with $r_{x,y,z} \in [-1, 1]$ uniform random numbers. We do not alter velocities and every copy keeps the velocity of the original particle. At small radii, $r < 0.2$ pc, we rotate the particles randomly about the z -axis otherwise the resulting orbits are too closely spaced. Our implementation of resampling conserves total particle number but not individually for the NCD and NCS. When a particle is re-sampled more than once all daughter particles inherit its affiliation to either the NCD or the NCS.

Particle re-sampling at work is illustrated in Figure 2. The top panel compares a final particle weight distribution of a model generated using NMAGIC without re-sampling with the peaked distribution of a corresponding model built including re-sampling. The model with a narrow weight distribution has a higher effective resolution and hence suffers less from shot noise than its counterpart with a broad distribution. Starting from a spherical particle population the NCD shown in the bottom panel is obtained by combining NMAGIC with re-sampling. The effective number of particles is defined as $N_{eff}/N = \overline{w^2}/\bar{w}^2$ (de Lorenzi et al. 2007). Then, the particle models shown in Figure 2 have $1 - N_{eff}/N = 0.67$ without re-sampling and $1 - N_{eff}/N = 9.8 \times 10^{-6}$ with re-sampling, *i.e.* re-sampling leads to $\sim 3 \times$ higher N_{eff} .

3.5 Run parameters

Based on our experience in previous work, we set the value of the force-of-change parameter $\epsilon = 8 \times 10^{-8}$ and the temporal smoothing parameter $\alpha = 2.1\epsilon$. We set the entropy parameter $\mu = 2 \times 10^{-6}$. (The parameters (ϵ, α, μ) are defined in Syer & Tremaine (1996) and de Lorenzi et al. (2009).) We used timesteps $\delta t = 673$ years, with χ^2 -M2M correction steps every 20 timesteps. For comparison, a circular orbit at $r = 13.4$ pc, which contains half the particle mass, takes 1.82 Myr.

4 DYNAMICAL MODELS

In this section we construct dynamical models for the central region of NGC 4244 to assess its intrinsic kinematics and to constrain the NC mass. We investigate axisymmetric, two-component models for different combinations of mass-to-light ratios, fitting the photometry and NIFS integral field kinematic data.

All models are constructed including re-sampling of particle coordinates as described in Section 3.4. In order to reduce computational cost, the bulk of the modelling is performed using 0.75M particles, with the gravitational potential calculated on the Cartesian grids and held fixed throughout. In these models trajectories are integrated with a standard leapfrog scheme with a fixed time step. The models

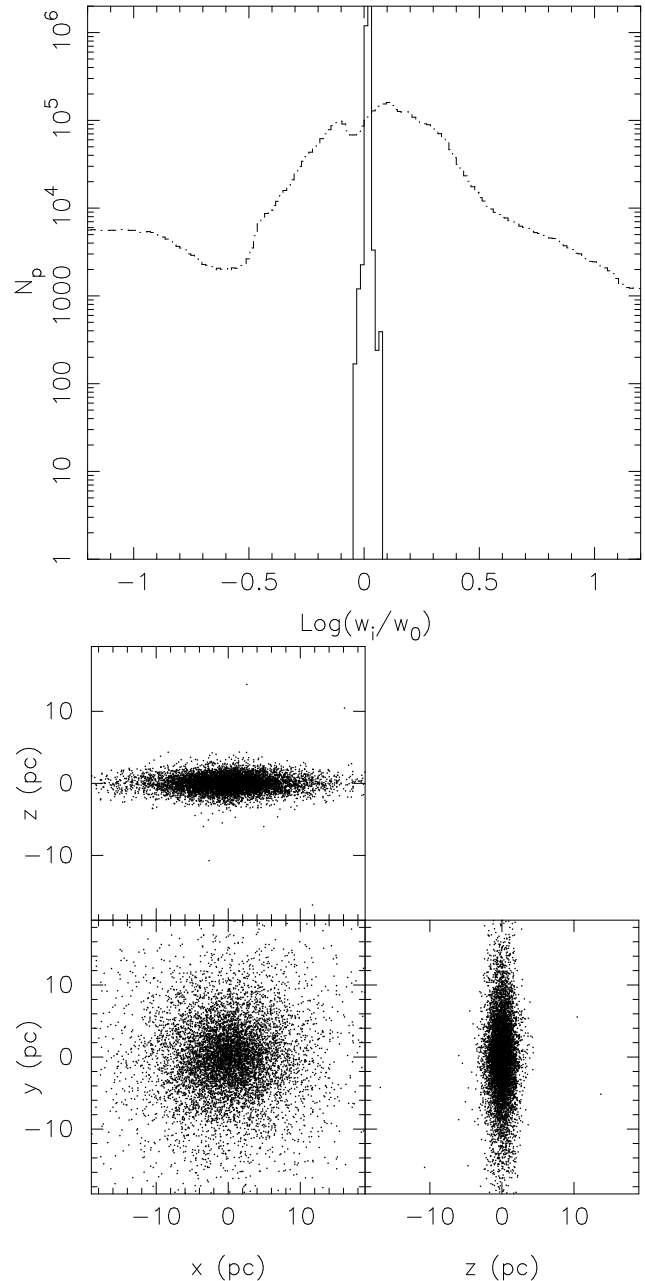


Figure 2. Top: comparison of the particle weight distribution of model M2 generated including re-sampling (solid line) and a corresponding model produced without re-sampling (dot-dashed line). Bottom: Distribution of a subset of NCD particles of the M2 model, generated using NMAGIC with re-sampling. The three panels show different projections of the particle coordinates. Note that the initial NCD model was spherical.

are constructed in a two step process. First, we start with the spherical isotropic 0.75M particle model and evolve it using NMAGIC to generate a particle realisation with desired luminosity distribution, fitting simultaneously but separately the NCS and NCD photometric constraints. Since only photometric (not kinematic) constraints are fit at this stage, the velocity scaling is arbitrary and only the ratio of M/L_{NCD} and M/L_{NCS} matters for the shape of the gravitational potential. In order to compute the gravitational po-

tential the ratio $(M/L_{\text{NCD}})/(M/L_{\text{NCS}})$ is fixed at 0.2/1.8. The resulting model then serves as a starting point to simultaneously fit both the photometric and kinematic constraints ($N_{\text{obs}} = 2365$ observables) for different combinations of M/L_{NCD} and M/L_{NCS} . During this adjustment phase, we typically evolve for 4M timesteps (2.7 Gyr) and apply 200K M2M correction steps. The particle system is then relaxed for a further 100K timesteps (67 Myrs) without changing particle weights. We refer to the final models as series M1. We vary M/L_{NCS} between 1.0 and 4.8, whereas we use values for M/L_{NCD} of 0.1, 0.2 and 0.4. The influence of the mass-to-light ratio of the MD on the quality of the fit is expected to be negligible; we therefore keep it constant at $M/L_{\text{MD}} = 0.7$ compatible with estimates from integrated colours.

The results are presented in Figure 3, which illustrates how the quality of the model fit changes with mass-to-light ratios. The top panel shows $\Delta\chi^2 = \chi^2 - \min\{\chi^2\}$, whereas $\Delta\chi^2_{\text{kin}}$ of the kinematic observables alone ($\Delta\chi^2$ "marginalised" over the A_{lm} 's) is shown in the bottom panel. The 68% confidence limits (1σ) are computed as $\sqrt{2N_{\text{obs}}}$ following van den Bosch & van de Ven (2009). These limits are $\Delta\chi^2 = 68.8$ and $\Delta\chi^2_{\text{kin}} = 27.0$, respectively.

Regardless of whether $\Delta\chi^2_{\text{kin}}$ or $\Delta\chi^2$ is used, the resulting best model has mass-to-light ratios $M/L_{\text{NCD}} = 0.4$ and $M/L_{\text{NCS}} = 1.4$. Note that the models with $M/L_{\text{NCD}} = 0.1$ or $M/L_{\text{NCD}} = 0.2$ and $M/L_{\text{NCS}} = 1.6$ reproduce the NIFS data with comparable quality and are in better agreement with $M/L_{\text{NCD}} = 0.1 - 0.25$ estimated from integrated colours (see Section 2.1) than is $M/L_{\text{NCD}} = 0.4$. Moreover, $M/L_{\text{NCD}} = 0.1$ also agrees with the estimates from Bruzual & Charlot models (Bruzual & Charlot 2003).

The range of acceptable NCS masses is estimated as the range for which $\Delta\chi^2$ ($\Delta\chi^2_{\text{kin}}$) is below 1σ confidence after "marginalising" over M/L_{NCD} . Although $\Delta\chi^2$ is the more appropriate quantity to discriminate between models because both photometric and kinematic constraints are imposed on the models, the allowed NCS mass ranges determined using either $\Delta\chi^2$ or $\Delta\chi^2_{\text{kin}}$ agree with each other. We obtain a NCS mass of $M_{\text{NCS}} = 1.6^{+0.5}_{-0.2} \times 10^7 M_{\odot}$ within ≈ 42.4 pc. This is almost an order of magnitude higher than the lower limit of $\sim 2.5 \times 10^6 M_{\odot}$ obtained from the observed velocity of an HII region at a projected distance of 19 pc from the NC center (Seth et al. 2006). The mass within ~ 15 pc is $1.0 \times 10^7 M_{\odot}$, which agrees with the mass within the same radius obtained from the JAM models in H11, $(1.1 \pm 0.2) \times 10^7 M_{\odot}$. The mass of the NCD is not as well constrained: we obtain $3.6 \times 10^5 M_{\odot}$ for $M/L_{\text{NCD}} = 0.1$ and $14.4 \times 10^5 M_{\odot}$ for $M/L_{\text{NCD}} = 0.4$.

At this point models with 6M particles are constructed starting from the spherical isotropic 6M particle initial conditions. We start by generating high resolution versions of models M1 with $M/L_{\text{NCD}} = 0.1$. We again use photometric followed by photometric+kinematic constraints. But now we replace the FFT method with a spherical harmonics potential solver in order to obtain higher spatial resolution at the centre. These models also use a Runge-Kutta time-integrator with adaptive timestep (using routine ODEINT of Press et al. (1992) with accuracy parameter 10^{-6}) to allow a comparison with the models which include a black hole, presented in the next section below. Since the potential is computed via an expansion in l, m spherical harmonics anal-

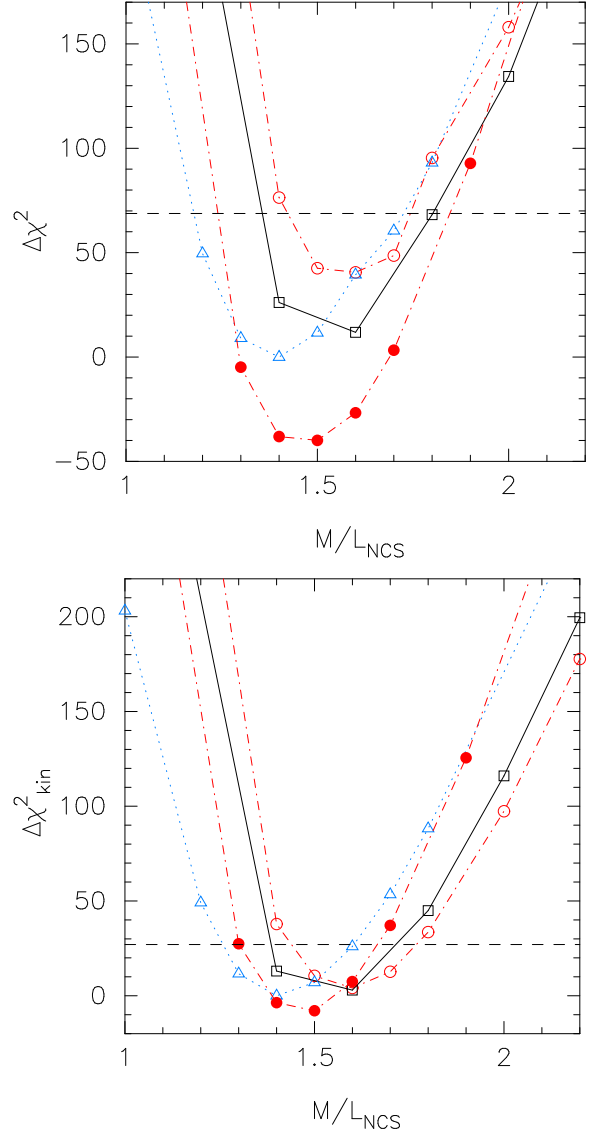


Figure 3. $\Delta\chi^2 = \chi^2 - \min\{\chi^2\}$ as a function of NCS and NCD K -band mass-to-light ratio. Upper panel: Total $\Delta\chi^2$ for the model fit to the photometric and kinematic target observables. Bottom panel: $\Delta\chi^2_{\text{kin}}$ of the kinematic observables only. Dashed horizontal lines correspond to 68% (1σ) confidence after van den Bosch & van de Ven (2009). Symbols are as follows: The M1 series for $M/L_{\text{NCD}} = 0.1, 0.2$ and 0.4 are shown as open (red) circles, (black) squares and (blue) triangles, joined by dot-dashed, solid and dotted lines, respectively. Models in series M2 are indicated by the solid circles joined by the red dot-dashed lines.

ogous to the photometric constraints, we include the same terms in the expansion of the potential as for the luminosity density (*i.e.* non-zero A_{lm}^{NCD} and A_{lm}^{NCS} , *cf.* also Section 3.3). The potential is recalculated after every M2M correction step. We refer to the resulting models as series M2.

The 6M particle models illustrate several interesting points. The NCS mass estimated using 6M particles agrees with the estimates presented above using the M1 models. This suggests that the inferred NCS mass is robust with respect to how the models have been constructed, in particular to the potential solver, integration scheme and number

of particles. Increasing the number of particles from M1 to M2 decreases χ^2_{kin} of the corresponding best models by only a small amount (if at all) with respect to the $\Delta\chi^2_{kin}$ confidence limit. This indicates that the model fit to the NIFS data is dominated by the uncertainties in the data while the contribution of shot noise to χ^2_{kin} is negligible. On the other hand, χ^2 is reduced considerably mainly due to a reduction in χ^2_{Alm} ¹. This suggests that χ^2_{Alm} is dominated by Poisson noise. Generally $\chi^2_{Alm} < N_{Alm}$ because of the temporal smoothing, and both the M1 and M2 models reproduce the photometric data very well.

We present the intrinsic kinematics of the best-fit model in series M2 in Figure 4. We computed the radial, tangential and vertical dispersions, σ_u , σ_v and σ_w respectively, and plot the anisotropies $\beta_\phi = 1 - (\sigma_v/\sigma_u)^2$ and $\beta_z = 1 - (\sigma_w/\sigma_u)^2$. In agreement with H11 we find that $\beta_z < 0$. Also V_{rms} has a central minimum. H11 found that the combination of these two properties provide important constraints on the amount of mass that the nuclear cluster could have accreted in the form of star clusters, as we shall also see below.

4.1 Adding intermediate mass black holes

Some galaxies are known to harbour both a NC and a massive black hole (Seth et al. 2008a; Graham & Spitler 2009; Neumayer & Walcher 2012). Since mass and anisotropy are degenerate with each other (Binney & Mamon 1982), we wish to explore how adding an IMBH might change β_z . We therefore also generate models including an IMBH at their centre with the aim of finding a robust upper IMBH mass limit compatible with the observations. We construct these models in a manner analogous to models M2 above, using a spherical harmonics potential solver in order to obtain higher spatial resolution at the centre. These models again use a Runge-Kutta time-integrator with adaptive timestep for higher accuracy in the vicinity of the IMBH. Using two-integral JAM models (Cappellari 2008) H11 obtained an upper limit of $M_\bullet \lesssim 10^5 M_\odot$ on any black hole that may be present. We revisit this estimate with our more general three-integral modelling.

The IMBH is represented by a Plummer potential with scale-length set to 0.02 pc. We generate models M3 to M8 for various IMBH mass fractions. The IMBH mass fractions $\zeta = M_\bullet/(M/L_{NCS} \times 10^5 M_\odot)$ are given in Table 2. For each series of models the black hole mass is then given as $M_\bullet = \zeta \times M/L_{NCS}$. The results of the models are presented in Figure 5, which illustrates how the quality of the model fit changes with M/L_{NCS} and ζ . The left panel shows $\Delta\chi^2 = \chi^2 - \min\{\chi^2\}$, whereas $\Delta\chi^2_{kin}$ of the kinematic observables alone is shown in the middle and right panels. The 68% confidence limits are as in the above *i.e.* $\Delta\chi^2 = 68.8$ and $\Delta\chi^2_{kin} = 27.0$.

As expected, the minimum χ^2 along a given line in Figure 5 shifts towards smaller M/L_{NCS} with increasing IMBH mass fraction (see especially the right panel of Figure 5). Each line in Figure 5 intersects the confidence limit (dashed horizontal line) twice (in the case of series M3 and M4 the modelling sets need to be extrapolated). The intersection with larger M/L_{NCS} corresponds to the largest admissible

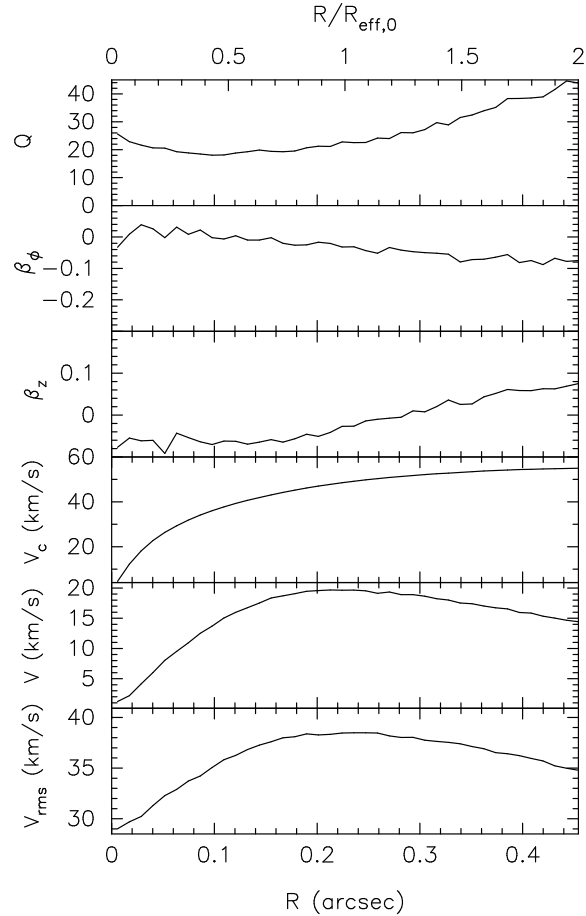


Figure 4. The intrinsic kinematics of the NC in the best-fit model in the M2 series. From bottom up we show the second moment of line-of-sight velocity V_{rms} , line-of-sight velocity V , the circular velocity V_c , the vertical anisotropy β_z , and the tangential anisotropy β_ϕ . The top row shows the Toomre- Q of the NCD only.

IMBH mass along each line. The largest IMBH mass compatible with the data would be obtained at a line that intersects the horizontal line only once, at its minimum χ^2 . Using $\Delta\chi^2_{kin}$ shown in the right panel of Figure 5, the dashed line with $M/L_{NCS} = 1.2$ leads to the IMBH mass upper limit of $M_\bullet = 5.0 \times 10^5 M_\odot$. This upper limit is larger than the one found in H11 using JAM models, presumably reflecting the greater orbital freedom presented by 3-integral versus 2-integral models.

If we use $\Delta\chi^2$ shown in the left panel of Figure 5 instead of $\Delta\chi^2_{kin}$, we find that even larger IMBH masses (up to a factor 2 or higher) are compatible with the data. Nonetheless, we use the more conservative IMBH mass range provided by the NIFS data alone.

Figure 6 shows a comparison of the best fit models in series M2 and M6 (indicated by the orange stars in the middle and right panels of Figure 5) with the integral field NIFS kinematic. The model fits to the NIFS data are excellent. χ^2_{kin} for the best models M2 and M6 are 194.715 and 207.532, respectively. Figure 7 shows a comparison of the best fit models in the M2 and M6 series with major-axis kinematic data extracted from the NIFS data. The

¹ We use the same MC A_{lm} errors as for models M1.

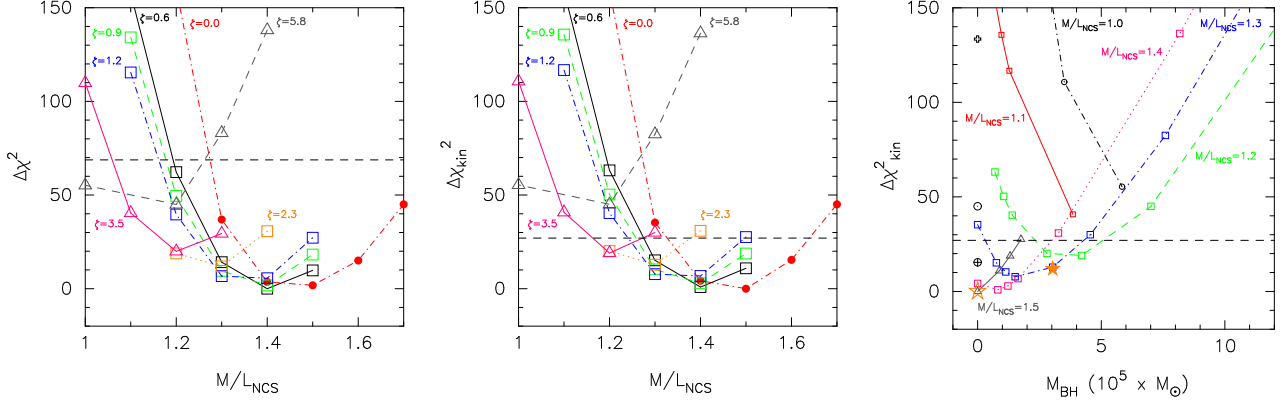


Figure 5. $\Delta\chi^2 = \chi^2 - \min\{\chi^2\}$ as a function of NCS mass-to-light ratio for various IMBH mass fractions $\zeta = M_{\bullet}/(M/L_{\text{NCS}})$. Left panel: Total $\Delta\chi^2$ for the model fit to the photometric and kinematic target observables. Middle panel: $\Delta\chi^2_{\text{kin}}$ of the kinematic observables only. Right panel: $\Delta\chi^2_{\text{kin}}$ as a function of M_{\bullet} instead of M/L_{NCS} . Dashed horizontal lines correspond to 68% (1σ) confidence after van den Bosch & van de Ven (2009). In the left and middle panels the symbols are as follows: The M2 series is shown as solid (red) circles joined by red dot-dashed lines. Models including a central IMBH are shown as open squares joined by (black) solid (M3), (green) dashed (M4), (blue) dot-dashed (M5) or (orange) dotted (M6) lines. The open triangles are for series M7 and M8. The M7 and M8 series are joined by (pink) solid and (grey) dashed lines respectively. IMBH mass fractions for models in the M3 to M8 series are given in Table 2. In the right panel the different symbols represent: circles joined by (black) dot-dashed line: $M/L_{\text{NCS}} = 1$, squares joined by (red) solid line: $M/L_{\text{NCS}} = 1.1$, squares joined by (green) dashed line: $M/L_{\text{NCS}} = 1.2$, squares joined by (blue) dot-dashed line: $M/L_{\text{NCS}} = 1.3$, squares joined by (pink) dotted line: $M/L_{\text{NCS}} = 1.4$, triangles joined by (grey) solid line: $M/L_{\text{NCS}} = 1.5$, (single) crossed circle: $M/L_{\text{NCS}} = 1.6$, (single) dotted circle: $M/L_{\text{NCS}} = 1.7$, (single) cross: $M/L_{\text{NCS}} = 1.9$, and (single) diamond: $M/L_{\text{NCS}} = 2.2$. The open and solid (orange) stars in the middle and right panels mark the best fit M2 and M6 models, respectively.

SERIES	$N_p (\times 10^6)$	M/L_{NCD}	M/L_{NCS}	$\zeta = \frac{M_{\text{BH}}}{(M/L_{\text{NCS}}) \times 10^5 M_{\odot}}$	POT.	INT.
M1	0.75	0.1, 0.2, 0.4	1.0 – 4.8	–	FFT	LEAPFROG
M2	6	0.1	1.0 – 2.2	–	SPH. HARM.	RUNGE-KUTTA
M3	6	0.1	1.1 – 1.5	0.6	SPH. HARM.	RUNGE-KUTTA
M4	6	0.1	1.1 – 1.5	0.9	SPH. HARM.	RUNGE-KUTTA
M5	6	0.1	1.1 – 1.5	1.2	SPH. HARM.	RUNGE-KUTTA
M6	6	0.1	1.2 – 1.4	2.3	SPH. HARM.	RUNGE-KUTTA
M7	6	0.1	1.0 – 1.3	3.5	SPH. HARM.	RUNGE-KUTTA
M8	6	0.1	1.0 – 1.4	5.8	SPH. HARM.	RUNGE-KUTTA

Table 2. Summary of the modelling runs. Columns from left to right are: Name of the series of models, number of particles, mass-to-light ratio of the NCD, mass-to-light ratio of the NCS, IMBH mass fraction ζ , the method used to compute the potential and the time integration scheme.

model kinematics are computed from a Gauss-Hermite fit to the line-of-sight velocity distribution in the corresponding Voronoi bins. To compute the temporally smoothed LOSVD, we use 27 bins in velocity within a range of width 300 km s^{−1}, centred on the corresponding NIFS line-of-sight velocity. Note that we did not fit the full LOSVD itself, instead we constrained the particle models using luminosity-weighted moments as described in Section 3.1.

5 N-BODY SIMULATIONS

Our best dynamical model without an IMBH is M2 with $M/L_{\text{NCS}} = 1.5$. After building this model we used it for a number of N -body experiments testing its stability and evolution by using it as initial conditions. The simulations, were evolved with PKDGRAV (Stadel 2001), an efficient, multi-stepping, parallel treecode. In all cases we use an opening angle $\theta = 0.7$. We used base timestep $\Delta t = 0.1$ Myr

and changed timesteps of individual particles such that $\delta t = \Delta t/2^n < \eta(\epsilon/a)^{1/2}$, where ϵ is the softening and a is the acceleration of the particle, with n as large as 29 allowed. We set $\eta = 0.03$, a quite conservative value.

5.1 Stability test

In constructing our dynamical model we have assumed that the NC in NGC 4244 is very likely axisymmetric. H11 found no evidence of non-axisymmetry in the NC of M33. Its PA is consistent with that of its main disc and its apparent ellipticity is consistent with a vertical flattening of $q = 0.7$, the average observed in the NCs of edge-on late-type galaxies (Seth et al. 2006). There is also only a small misalignment between photometric and kinematics major axis. At present, M33 is the only galaxy in which the axial symmetry of the NC can be determined.

Our first N -body simulation therefore tests the stability

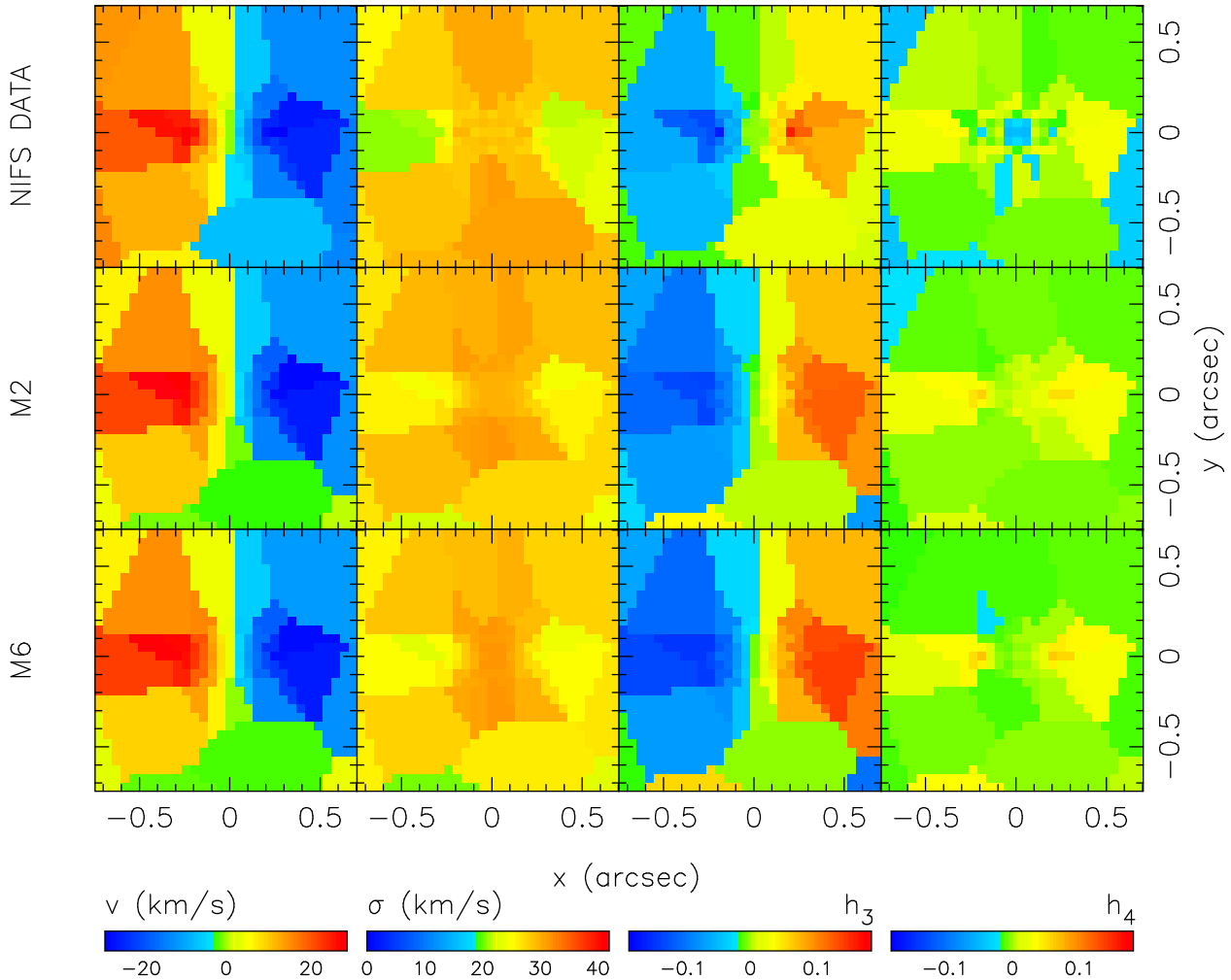


Figure 6. Symmetrised NIFS integral-field kinematic data within $\pm 0.7''$ of the central region of NGC 4244 (top row) compared with corresponding luminosity-weighted data extracted from the best-fit models in series M2 (middle row) and M6 with $M/L_{\text{NCD}} = 0.1$, $M/L_{\text{NCS}} = 1.3$ and $M_{\text{bh}} = 3.0 \times 10^5 M_{\odot}$ (bottom row). These models are indicated by the open and solid orange stars, respectively, in the right panel of Figure 5. From left to right are shown: line-of-sight velocity v , line-of-sight velocity dispersion σ and higher order Gauss-Hermite moments h_3 and h_4 .

of the model against non-axisymmetric perturbations, particularly the bar instability, which plagues rapidly rotating systems. After evolving the best fit model in series M2 for 50 Myr (the rotation period at 5 pc being 0.63 Myr), the model remained axisymmetric with no hint of a bar or spirals. The top panel of Figure 4 plots the Toomre- $Q = \sigma_u \kappa / (3.36 G \Sigma)$ of the NCD, where κ is the epicyclic radial frequency, G is the gravitational constant and Σ is the surface density. The stability of the system stems from the high Toomre- Q of the NCD, which is everywhere greater than 10.

5.2 Accretion simulations

H11 explored the hypothesis that NC formation is a result of star cluster (SC) accretion. They showed that the observed kinematics of the NC in NGC 4244 are not consistent with accretion of more than $\sim 50\%$ of its mass in the form of SCs. Specifically, once the accreted mass fraction exceeded this value the resulting central V_{rms} was no longer a minimum. We will see here too that V_{rms} starts to lose its central

minimum once the accreted mass fraction becomes too large, and our constraint is even more stringent than that of H11. On the other hand, H11 showed that the negative β_z of the NC was only possible if it accreted $\gtrsim 10\%$ of its mass as SCs on highly inclined orbits. Those simulations assumed SCs accreting onto a pre-existing NC, either as a NCD or as an isotropic NCS. Therefore we next subject our best-fitting model of the NC to SC accretions.

In order to permit the model star clusters to sink to the centre via dynamical friction, we introduce the best fit model in the M2 series inside a particle main disc with an exponential profile, because NGC 4244 is a late-type, bulgeless galaxy. We use the same model for the MD as did H11, *i.e.* four million multi-mass particles with masses ranging from $7M_{\odot}$ within the inner 20 pc increasing to $1.2 \times 10^7 M_{\odot}$ in the disc's outskirts. The distributions of masses and softening of the main disc particles are shown in Figure 6 of H11; the softening is related to particle mass via $\epsilon_p \propto m_p^{1/3}$.

We accrete three of the model SCs described in H11 which we term G1, G2 and G3 in order of increasing mass.

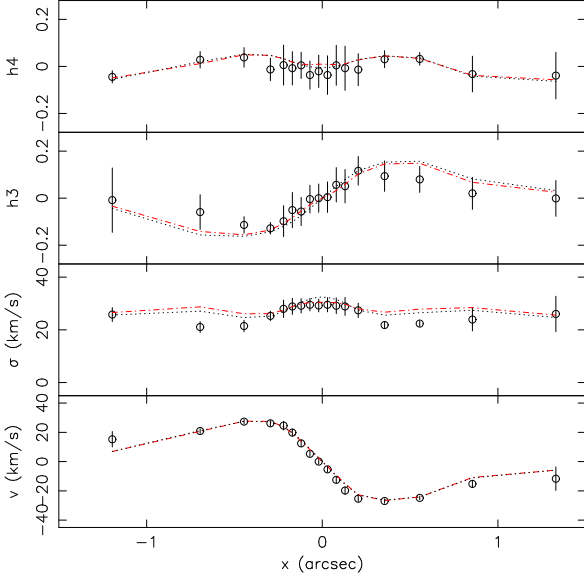


Figure 7. Comparison of the best-fit models in series M2 and M6 (indicated by the open and solid orange stars in Figure 5) to the kinematic data along the major-axis extracted from the NIFS data. Models and data are shown as lines and open circles, respectively, with M2 indicated by the dot-dashed (red) line and M6 by the dotted (black) line. From bottom to top are shown: velocity v , velocity dispersion σ , and Gauss-Hermite moments h_3 and h_4 . The model kinematic data were computed using a Gauss-Hermite fit to the velocity distribution along the line-of-sight.

Their properties are listed in Table 3. As in H11, we define the concentration of each star cluster as $c \equiv \log(R_{\text{eff}}/R_c)$ where R_{eff} is the half mass radius (effective radius) and R_c is the core radius, where the surface density drops to half of the central. These were allowed to accrete onto the NC starting from circular orbits at 50 pc from the centre. We start the SCs from 4 different inclinations relative to the NCD: 0° , 30° , 60° , and 90° . The SCs require about 40 Myrs to accrete onto the NC.

The results of these accretion simulations are shown in Figure 8. The low density star cluster G1 is disrupted at ~ 8 pc from the centre. Thus it barely perturbs the kinematics of the NC. However we note that there is a general tendency for β_z to increase slightly within R_{eff} , suggesting that even this mild $\sim 1\%$ mass accretion can alter the kinematics. The more massive, denser, clusters G2 and G3, both of which sink all the way to the centre, perturb the kinematics much more. In all cases β_z increases; for G2 β_z averaged within R_{eff} is nearly zero, while $\beta_z > 0$ everywhere within R_{eff} when G3 is accreted.

Accreting G3 (which has a mass $\sim 13\%$ that of the NC) also raises the central V_{rms} . Although V_{rms} at the centre remains smaller than at R_{eff} , there does not seem to be much room for further significant accretions without making V_{rms} centrally peaked, unlike the observations. This is likely to hold also if this mass fraction arrives as many smaller star clusters, provided that the star clusters are dense enough that some fraction of their stars survives all the way to the centre of the NC.

Model	M_* [$\times 10^5 M_\odot$]	R_{eff} [pc]	c	H11 name
G1	2	1.11	0.12	C4
G2	6	1.11	0.16	C5
G3	20	2.18	0.12	C3

Table 3. The star clusters used in the accretion simulations. M_* is the stellar mass of the SC, R_{eff} is the effective (half-mass) radius, and c is the concentration (defined in the text). For comparison, the last column lists the name used for the model in H11.

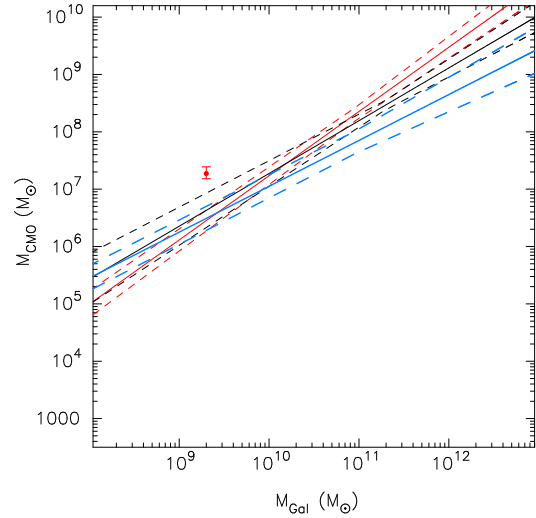


Figure 9. Mass of the NC of NGC 4244 versus the mass of the host galaxy compared with the $M_{\text{CMO}} - M_{\text{gal}}$ relations of Ferrarese et al. (2006). The solid red and black lines show the correlations for NCs and SMBHs in early-type galaxies, respectively, with 1σ confidence levels shown as dashed lines. The blue lines show the relation of Scott & Graham (2012).

6 DISCUSSION AND CONCLUSIONS

We have performed a dynamical study of the nuclear cluster in the edge-on spiral galaxy NGC 4244 taking into account different morphological components, which are the galaxy main disc (MD), nuclear cluster disc (NCD) and nuclear cluster spheroid (NCS). We have constructed axisymmetric dynamical particle models accounting for the MD, the NCD and the NCS. We find a total NCS mass $M_{\text{NCS}} = 1.6^{+0.5}_{-0.2} \times 10^7 M_\odot$ within approximately 42.4 pc ($2''$). Both the fits of Seth et al. (2005a) and of Fry et al. (1999) show that there is no obvious bulge component in NGC 4244. Using the 2MASS Large Galaxy Atlas (Jarrett et al. 2003) K -band magnitude, the total luminosity of the galaxy is $3.2 \times 10^9 L_\odot$, and thus the galaxy stellar mass is $2 \times 10^9 M_\odot$. Figure 9 plots the NC mass compared with the $M_{\text{CMO}} - M_{\text{gal}}$ relation. The NC sits above this relation.

6.1 Vertical anisotropy

The kinematics are moderately tangentially anisotropic inside R_{eff} with an anisotropy parameter $\beta_z \sim -0.1$. This is

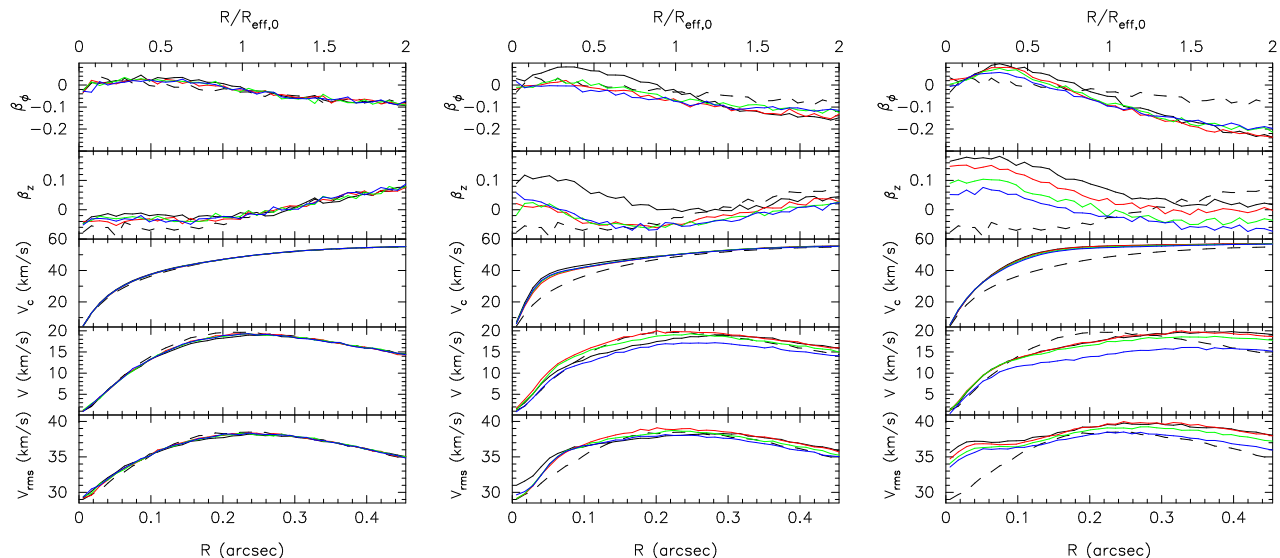


Figure 8. The effect of accreting star clusters onto the NC in NGC 4244. From left to right these show the effect of accreting SCs G1, G2 and G3. The black, red, green and blue solid lines show SCs accreting from 0° , 30° , 60° and 90° , respectively. The dashed line shows the initial NC.

in good agreement with the JAM models of H11. H11 showed that $\beta_z < 0$ requires high-inclination infall of star clusters onto a pre-existing nuclear cluster. In our accretion simulations onto a more realistic model of the NC we found that even the accretion of a star cluster of just 13% the mass is enough to erase the vertical anisotropy. This raises questions about whether such anisotropy can be due to accretion at all. It also hints that, unless we are observing the NC of NGC 4244 at a special time, it cannot sustain accretion of $\gtrsim 10\%$ mass as suggested by H11.

We therefore tested whether the assumption of a perfectly edge-on nuclear cluster may bias the modelled vertical anisotropy to negative values if the real inclination is somewhat smaller. The smallest inclination at which we were able to deproject the NCD photometry was 83° . Using a model deprojected at this assumed inclination and the observed kinematics, we built NMAGIC models assuming $M/L_{NCS} = 1.5$ starting from the best-fit edge-on model M2. The dashed black lines in Figure 10 show that the 2-D anisotropy, $\beta_z = 1 - \sigma_z^2/\sigma_R^2$, and 3-D anisotropy, $B_z = 1 - 2\sigma_z^2/(\sigma_R^2 + \sigma_\phi^2)$, are barely changed compared to the edge-on case (solid black lines) and remain negative. Thus a negative vertical anisotropy is not an artifact of assuming the nuclear cluster is perfectly edge-on.

We finally explore whether the recovered β_z changes if we include IMBHs in the models. In Figure 10 we plot both the vertical anisotropies for vary M_\bullet . While increasing M_\bullet raises the vertical anisotropy, it still remains negative within R_{eff} . We conclude that the NC must be vertically anisotropic even if a black hole were present.

6.2 Summary

We have built dynamical models of the NC in the nearby, edge-on late-type galaxy NGC 4244. Using particle re-sampling, we were able to obtain a narrow distribution of weights in our NMAGIC models allowing us to use the mod-

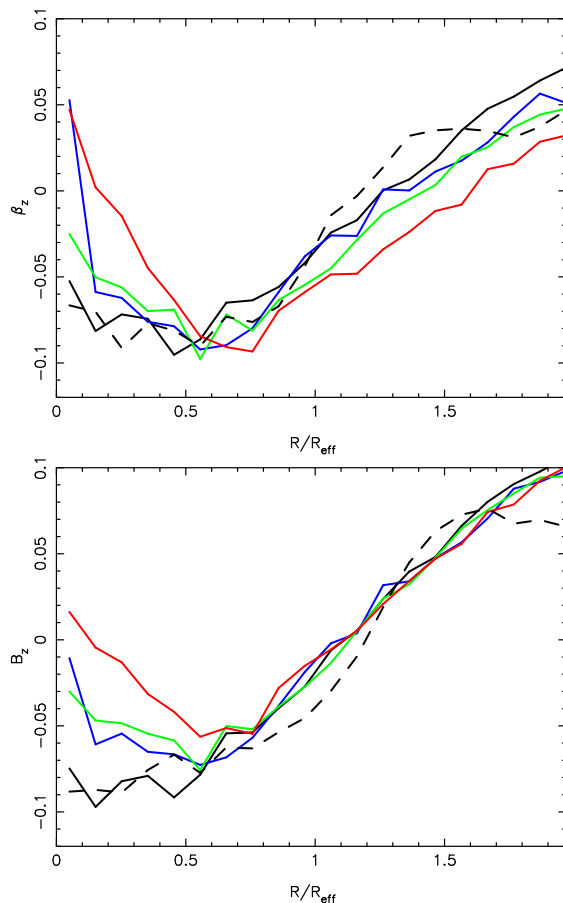


Figure 10. Profiles of 2-D (top) and 3-D (bottom) vertical anisotropy. The black, blue, green and red lines correspond to $M_\bullet = 0, 0.8, 1.23$, and $3.0 \times 10^5 M_\odot$, respectively. The dashed lines correspond to assuming that the nuclear cluster is inclined at 83° instead of being perfectly edge-on.

els as initial conditions in N -body simulations. Our results can be summarised as follows:

- We find a mass of the spheroidal component of the NC, $M_{\text{NCS}} = 1.6^{+0.5}_{-0.2} \times 10^7 M_{\odot}$ within 42.4 pc. The mass within 15 pc is $\sim 1.0 \times 10^7 M_{\odot}$, in very good agreement with the value estimated by Hartmann et al. (2011) using two-integral JAM models. This mass puts the nuclear cluster above the $M_{\text{NC}}\text{--}M_{\text{Gal}}$ relation.
- The mass of the bluer disc component of the nuclear cluster is less well constrained and covers the range $3.6 \times 10^5 M_{\odot} \lesssim M_{\text{NCD}} \lesssim 14.4 \times 10^5 M_{\odot}$.
- Our three-integral models are consistent with no black hole as well as with a black hole at least as massive as $4.6 \times 10^5 M_{\odot}$. This upper limit is larger than the one allowed by two-integral JAM models.
- Simulations show that the model without a black hole is stable against axisymmetric perturbations. This stability derives from the large Toomre- Q of the system.
- Regardless of whether a black hole is present or not, red and of whether the nuclear cluster is perfectly edge-on or not, β_z and B_z are both negative. Accretion of a star cluster of as little as 13% by mass is enough to drive β_z to positive values, regardless of the orbital geometry. It remains unclear, therefore, how $\beta_z < 0$ arose.

ACKNOWLEDGMENTS

The NMAGIC models in this paper were run on Albert, the supercomputer at the University of Malta. The simulations were run on Albert, on the High Performance Computer Facility at the University of Central Lancashire and on the COSMOS Consortium supercomputer within the DIRAC Facility jointly funded by STFC, the Large Facilities Capital Fund of BIS. Additional low resolution test models were run on the old linux cluster of the dynamics group at MPE.

REFERENCES

- Adams, F. C., Graff, D. S., Mbonye, M., & Richstone, D. O. 2003, *ApJ*, 591, 125
- Adams, F. C., Graff, D. S., & Richstone, D. O. 2001, *ApJ*, 551, L31
- Bekki, K. 2007, *Publications of the Astronomical Society of Australia*, 24, 77
- Bekki, K., Couch, W. J., & Shioya, Y. 2006, *ApJ*, 642, L133
- Bell, E. F., McIntosh, D. H., Katz, N., & Weinberg, M. D. 2003, *ApJS*, 149, 289
- Binney, J., & Mamon, G. A. 1982, *MNRAS*, 200, 361
- Böker, T., Laine, S., van der Marel, R. P., Sarzi, M., Rix, H.-W., Ho, L. C., & Shields, J. C. 2002, *AJ*, 123, 1389
- Böker, T., Sarzi, M., McLaughlin, D. E., van der Marel, R. P., Rix, H.-W., Ho, L. C., & Shields, J. C. 2004, *AJ*, 127, 105
- Bruzual, G., & Charlot, S. 2003, *MNRAS*, 344, 1000
- Burkert, A., & Silk, J. 2001, *ApJ*, 554, L151
- Cappellari, M. 2008, *MNRAS*, 390, 71
- Capuzzo-Dolcetta, R., & Miocchi, P. 2008, *MNRAS*, 388, L69
- Côté, P., Piatek, S., Ferrarese, L., Jordán, A., Merritt, D., Peng, E. W., Hasegan, M., Blakeslee, J. P., Mei, S., West, M. J., Milosavljević, M., & Tonry, J. L. 2006, *ApJS*, 165, 57
- Davidge, T. J., & Courteau, S. 2002, *AJ*, 123, 1438
- de Lorenzi, F., Debattista, V. P., Gerhard, O., & Sambhus, N. 2007, *MNRAS*, 376, 71
- de Lorenzi, F., Gerhard, O., Coccato, L., Arnaboldi, M., Capaccioli, M., Douglas, N. G., Freeman, K. C., Kuijken, K., Merrifield, M. R., Napolitano, N. R., Noordermeer, E., Romanowsky, A. J., & Debattista, V. P. 2009, *MNRAS*, 395, 76
- de Lorenzi, F., Gerhard, O., Saglia, R. P., Sambhus, N., Debattista, V. P., Pannella, M., & Méndez, R. H. 2008, *MNRAS*, 385, 1729
- Debattista, V. P., & Sellwood, J. A. 2000, *ApJ*, 543, 704
- Dehnen, W. 2009, *MNRAS*, 395, 1079
- Di Matteo, T., Springel, V., & Hernquist, L. 2005, *Nature*, 433, 604
- Erwin, P., & Gadotti, D. 2010, in *American Institute of Physics Conference Series*, Vol. 1240, American Institute of Physics Conference Series, ed. V. P. Debattista & C. C. Popescu, 223–226
- Erwin, P., & Gadotti, D. A. 2012a, *Advances in Astronomy*, 2012
- . 2012b, *Advances in Astronomy*, 2012
- Ferrarese, L., Côté, P., Dalla Bontà, E., Peng, E. W., Merritt, D., Jordán, A., Blakeslee, J. P., Hasegan, M., Mei, S., Piatek, S., Tonry, J. L., & West, M. J. 2006, *ApJ*, 644, L21
- Ferrarese, L., & Merritt, D. 2000, *ApJ*, 539, L9
- Fry, A. M., Morrison, H. L., Harding, P., & Boroson, T. A. 1999, *AJ*, 118, 1209
- Gebhardt, K., Bender, R., Bower, G., Dressler, A., Faber, S. M., Filippenko, A. V., Green, R., Grillmair, C., Ho, L. C., Kormendy, J., Lauer, T. R., Magorrian, J., Pinkney, J., Richstone, D., & Tremaine, S. 2000, *ApJ*, 539, L13
- Gerhard, O. E. 1991, *MNRAS*, 250, 812
- . 1993, *MNRAS*, 265, 213
- Graham, A. W. 2012, *MNRAS*, 2608
- Graham, A. W., Onken, C. A., Athanassoula, E., & Combes, F. 2011, *MNRAS*, 48
- Graham, A. W., & Spitler, L. R. 2009, *MNRAS*, 397, 2148
- Greene, J. E., Peng, C. Y., Kim, M., Kuo, C.-Y., Braatz, J. A., Violette Impellizzeri, C. M., Condon, J. J., Lo, K. Y., Henkel, C., & Reid, M. J. 2010, *ApJ*, 721, 26
- Haehnelt, M. G., & Kauffmann, G. 2000, *MNRAS*, 318, L35
- Hartmann, M., Debattista, V. P., Seth, A., Cappellari, M., & Quinn, T. R. 2011, *MNRAS*, 418, 2697
- Hockney, R. W., & Eastwood, J. W. 1988, *Computer simulation using particles* (Bristol: Hilger, 1988)
- Jahnke, K., & Macciò, A. V. 2011, *ApJ*, 734, 92
- Jarrett, T. H., Chester, T., Cutri, R., Schneider, S. E., & Huchra, J. P. 2003, *AJ*, 125, 525
- Johansson, P. H., Naab, T., & Burkert, A. 2009, *ApJ*, 690, 802
- Kazantzidis, S., Mayer, L., Colpi, M., Madau, P., Debattista, V. P., Wadsley, J., Stadel, J., Quinn, T., & Moore, B. 2005, *ApJ*, 623, L67
- King, A. 2003, *ApJ*, 596, L27
- Leigh, N., Böker, T., & Knigge, C. 2012, *ArXiv e-prints*

- Lotz, J. M., Telford, R., Ferguson, H. C., Miller, B. W., Stiavelli, M., & Mack, J. 2001, *ApJ*, 552, 572
- Magorrian, J. 1999, *MNRAS*, 302, 530
- McLaughlin, D. E., King, A. R., & Nayakshin, S. 2006, *ApJ*, 650, L37
- Milosavljević, M. 2004, *ApJ*, 605, L13
- Miralda-Escudé, J., & Kollmeier, J. A. 2005, *ApJ*, 619, 30
- Murray, N., Quataert, E., & Thompson, T. A. 2005, *ApJ*, 618, 569
- Neumayer, N., & Walcher, C. J. 2012, *ArXiv e-prints*
- Press, W. H., Teukolsky, S. A., Vetterling, W. T., & Flannery, B. P. 1992, *Numerical recipes in FORTRAN. The art of scientific computing* (Cambridge: University Press, —c1992, 2nd ed.)
- Rossa, J., van der Marel, R. P., Böker, T., Gerssen, J., Ho, L. C., Rix, H.-W., Shields, J. C., & Walcher, C.-J. 2006, *AJ*, 132, 1074
- Rybicki, G. B. 1987, in *IAU Symp. 127: Structure and Dynamics of Elliptical Galaxies*, ed. P. T. de Zeeuw, 397–+
- Sazonov, S. Y., Ostriker, J. P., Ciotti, L., & Sunyaev, R. A. 2005, *MNRAS*, 358, 168
- Schinnerer, E., Böker, T., & Meier, D. S. 2003, *ApJ*, 591, L115
- Scott, N., & Graham, A. W. 2012, *ArXiv e-prints*
- Sellwood, J. A. 2003, *ApJ*, 587, 638
- Sérsic, J. L. 1968, *Atlas de galaxias australes* (Cordoba, Argentina: Observatorio Astronomico, 1968)
- Seth, A., Agüeros, M., Lee, D., & Basu-Zych, A. 2008a, *ApJ*, 678, 116
- Seth, A. C., Blum, R. D., Bastian, N., Caldwell, N., & Debattista, V. P. 2008b, *ApJ*, 687, 997
- Seth, A. C., Dalcanton, J. J., & de Jong, R. S. 2005a, *AJ*, 129, 1331
- . 2005b, *AJ*, 130, 1574
- Seth, A. C., Dalcanton, J. J., Hodge, P. W., & Debattista, V. P. 2006, *AJ*, 132, 2539
- Silk, J., & Rees, M. J. 1998, *A&A*, 331, L1
- Springel, V., Di Matteo, T., & Hernquist, L. 2005, *MNRAS*, 361, 776
- Stadel, J. G. 2001, *Ph.D. Thesis*, University of Washington
- Syer, D., & Tremaine, S. 1996, *MNRAS*, 282, 223
- Tremaine, S. D., Ostriker, J. P., & Spitzer, Jr., L. 1975, *ApJ*, 196, 407
- van den Bosch, R. C. E., & van de Ven, G. 2009, *MNRAS*, 398, 1117
- van der Kruit, P. C., & Searle, L. 1981, *A&A*, 95, 105
- van der Marel, R. P., & Franx, M. 1993, *ApJ*, 407, 525
- Walcher, C. J., Böker, T., Charlot, S., Ho, L. C., Rix, H.-W., Rossa, J., Shields, J. C., & van der Marel, R. P. 2006, *ApJ*, 649, 692
- Wehner, E. H., & Harris, W. E. 2006, *ApJ*, 644, L17